Article Identifier
DOI: 10.22032/dbt.58683
URN: urn:nbn:de:gbv:ilm1-2023isc-009:9

60th ILMENAU SCIENTIFIC COLLOQUIUM
Technische Universität Ilmenau, 4 – 8 September 2023
URN: urn:nbn:de:gbv:ilm1-2023isc:1

A LASER DILATOMETER SETUP TO CHARACTERIZE DIMENSIONALLY STABLE MATERIALS FROM 100 K TO 300 K

Ines Hamann[1], Lee Kumanchik[1,2], Gudrun Wanner[3], Martin Gohlke[4], Josep Sanjuan[1], Claus Braxmaier[1,2]

[1] Deutsches Zentrum für Luft- und Raumfahrt, Institute of Quantum Technologies (DLR QT), Ulm, Germany
[2] Ulm University, Institute of Microelectronics, Ulm, Germany
[3] Institute for Gravitational Physics of the Leibniz Universität Hannover and Max Planck Institute for Gravitational Physics (Albert Einstein Institute), Hannover, Germany
[4] Deutsches Zentrum für Luft- und Raumfahrt, Institute of Space Systems (DLR RY), Bremen, Germany

ABSTRACT

In our structural dimensional metrology laboratory, we implemented a setup to determine coefficients of thermal expansions (CTE) of ultra-stable materials at temperatures from 300 K down to 100 K. Such low CTE materials are important for dimensionally stable structures in space and terrestrial applications, e. g. to enable precise measurements. This CTE characterization is done in the 10 ppb/K ($10 \cdot 10^{-9}$ K^{-1}) range by applying small temperature variation around dedicated absolute temperatures. In order to accommodate arbitrary sample materials, we bounce light off mirrors attached to the sample by custom mounts. The light and therefore the thermal-induced length variations is then analyzed by an interferometer with sub-nanometer sensitivity. Here, we present a more detailed investigation of a process during sample measurements using differential wavefront sensing (DWS).

Index Terms - dilatometry, differential wavefront sensing, CTE

1. INTRODUCTION

Thermal dilatometry is a common technique to determine the coefficient of thermal expansion (CTE). We have developed an interferometric based laser dilatometer, which is free of stick-slip issues present in classic push-rod dilatometers.
Our setup is an upgrade of a measurement facility for CTE determination at room temperature with demonstrated measurements of CTE values down to 10 ppb/K [1]. In the temperature range between 140 K and 250 K we showed a measurement uncertainty of 20 ppb/K to 80 ppb/K [2]. In our previous publications [3][4] we investigated a silicon sample at 285 K with temperature peak-to-peak variation of approximately 4 K. The tilt-to-length (TTL) coupling in our setup was simulated with a simulation model based on IfoCAD [5][6] and the CTE result was corrected by using signals derived from differential wavefront sensing (DWS).
The DWS signal of one of the quadrant photo detectors showed an unexpected pattern with higher order frequency components compared to our excitation signal. In this work we included a further analysis to the frequency components present in our setup.
The following sections include the setup description, the setup analysis and a conclusion.

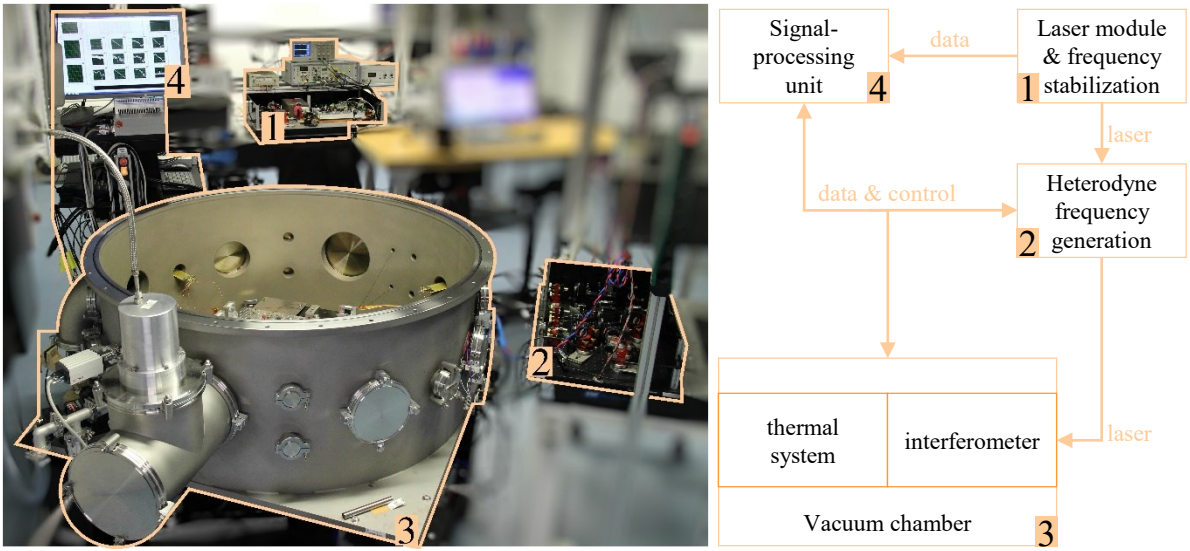

Figure 1: Overview of the dilatometer subsystems in our laboratory with 1: Laser module with frequency stabilization, 2: Heterodyne frequency generation, 3: Vacuum chamber including interferometer and thermal system and 4: Signal-processing unit

2. SETUP DESCRIPTION

Our dilatometer setup is divided into four subsystems. They are shown in Figure 1 and a detailed description can be found in [2][4]. In this setup we use a laser module providing outputs at wavelengths of 1064 nm and 532 nm. The laser frequency is stabilized using the 532 nm hyperfine transition of molecular iodine [7]. The light at 1064 nm is used for the measurement. It is split into two beams with each beam shifted in frequency by acousto-optic modulators. The difference between the shifting frequencies is 10 kHz, which is the beat frequency later detected. Using optical fibers, two beams are guided to the vacuum chamber, which comprises the heterodyne interferometer and thermal system. The signal-processing unit includes the electrical drivers as well as optical and electrical read-out, including the phasemeter based on single bin discrete Fourier transform.
With this setup we are able to determine the linear CTE, which is calculated as

$$\alpha = \frac{1}{L} \cdot \frac{\Delta L}{\Delta T} \tag{1}$$

with ΔL, ΔT the length and temperature variation, respectively and L is the absolute length of the sample, which is defined by the mirrors M1 and M2 clamped inside the sample (Figure 2). While the temperature is changing, the length of the sample is also changing. Consequently, the distance between the mirrors inside the sample is changing too. The two beams were guided to the sample and reflected at M1 and M2. These reflected beams at frequency f_1 are superimposed on quadrant detectors (QPDs) with two beams at frequency f_2. The interference of the beams generates a signal at 10 kHz. The signal-processing unit extracts the amplitude a_j and phase ϕ_j of each QPD segment j, which are used to calculate the length variation as [3][4][8]

$$\Delta L = \frac{\lambda}{4\pi}\left(\arg\left(\sum_{j=1}^{4} a_j \exp(\mathrm{i}\phi_j)\right) - \arg\left(\sum_{j=5}^{8} a_j \exp(\mathrm{i}\phi_j)\right)\right) \tag{2}$$

and tilt signals based on the DWS method [3][4][5][9]

$$\eta_1 = \arg\left(\frac{a_2\exp(\mathrm{i}\phi_2) + a_3\exp(\mathrm{i}\phi_3)}{a_1\exp(\mathrm{i}\phi_1) + a_4\exp(\mathrm{i}\phi_4)}\right)$$
$$\eta_2 = \arg\left(\frac{a_5\exp(\mathrm{i}\phi_5) + a_8\exp(\mathrm{i}\phi_8)}{a_6\exp(\mathrm{i}\phi_6) + a_7\exp(\mathrm{i}\phi_7)}\right) \qquad (3)$$

with η_1 at QPD1 and η_2 at QPD2 indicating the angle between the reference and measurement beam. Both signals have no unit and will be used with arbitrary units (a.u.) throughout this publication.
Equation (3) allow us to calculate yaw-induced motions in our setup that eventually limit the accuracy of the measurement due to TTL coupling. Vertical tilts from pitch-induced motions can be neglected based on our setup design.

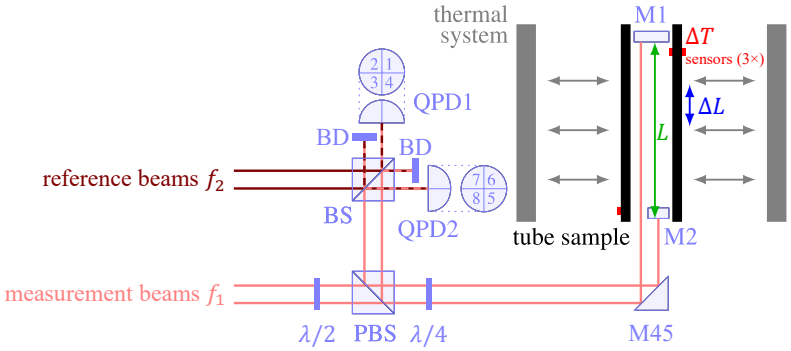

Figure 2: Schematic of the interferometer and thermal system with measurement beams f_1 passing half-wave plate $\lambda/2$, polarizing beam splitter PBS, quarter-wave plate $\lambda/4$ and 45° mirror M45. After interacting with the sample's mirrors M1 and M2, the reflected beams are passing again M45, $\lambda/4$, reflected in PBS and are superimposed with the reference beams f_2 at beam splitter BS and detected at quadrant photo detectors QPD1 and QPD2 (unused beams dumped at BDs). The distance between M1 and M2 defines the nominal length L, whose variation ΔL is caused by a temperature variation ΔT induced by the thermal system and measured by Pt100 sensors. (Original from [1]).

3. SETUP ANALYSIS

To determine the CTE value of a sample material we use tube shaped samples with an overall length from 60 mm to 120 mm and an outer diameter of 28 mm to fit into the sample support and thermal system. To clamp our mirror mounts inside the tube we need an inner tube diameter of 20 mm. These mirrors then define the nominal length L measured by interferometer, which is slightly different from the actual length of the sample tube. To derive $\Delta L/\Delta T$ for Equation (1), the interferometer measures the length variation while the thermal system is inducing a temperature variation in the sample. A detailed description can be found in previous publications [2][4]. We used a single-crystal silicon sample to test our CTE measurement procedure. Correcting the length variation from tilt-to-length (TTL) coupling has led to a CTE bias improvement from approximately 7% to less than 1%. One issue within the estimation process was that not all relevant signals showed a sinusoidal pattern as expected when using a thermal sinusoidal excitation.

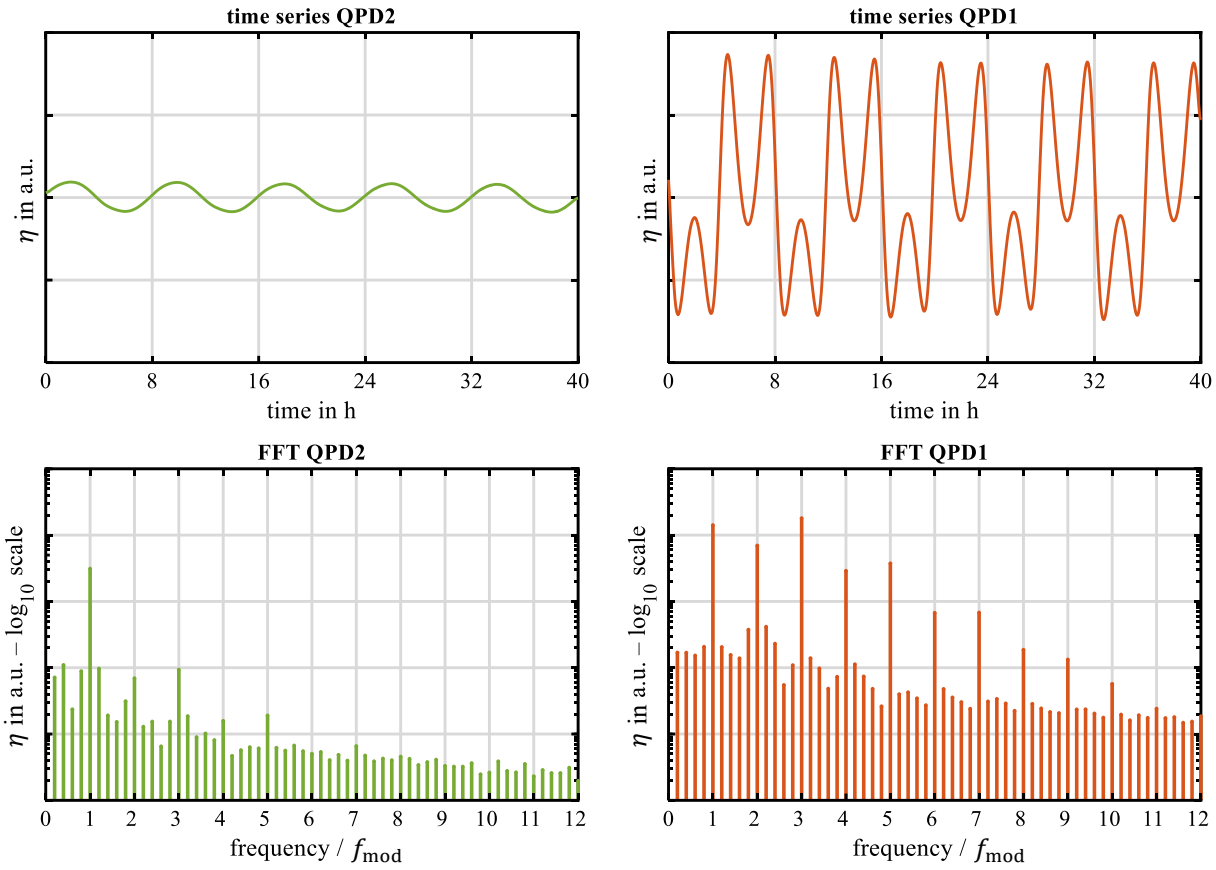

Figure 3: DWS signals detected by QPD2 (left) and QPD1 (right) while modulation the temperature (stabilized laser frequency). The upper plots show the time-domain signals while the lower plots show the FFT amplitude spectra. The modulation is driven at $f_{\mathrm{mod}} = 34.72$ µHz during $\Delta L/\Delta T$ characterization: QPD2's signal shows the expected modulation frequency with noise contribution from the system. In amplitude spectra, higher harmonics are distinguishable from the noise floor up to 5 with highest amplitude at 1. QPD1's signal show higher order frequency components. The FFT conversion shows higher harmonics up to 10 with highest amplitude at 3rd harmonics. Harmonics at 2, 4, 6 are smaller than corresponding odd components 1, 3, 5, 7. Overall, the noise floor of QPD1 is higher than the noise floor of QPD2. (Data from [3][4]).

3.1 Frequency domain analysis

To analyze this unexpected behavior, we focus on plots over frequency. Fast Fourier transform (FFT) is a suitable tool to transfer DWS time domain signals. We present the time-domain signal for orientation together with the FFT spectra of both DWS signals. All axes in Figure 3 and Figure 4 were adjusted in a way to simplify comparisons: *x*-axes in time-domain display time in hour or seconds based on cycling time. To overcome this in frequency domain: The *x*-axis was normalized by the modulation frequency used in the scenario. The corresponding *y*-axes are all scaled to the same limits to emphasize amplitude ratios between signals.

In Figure 3, the signals were detected while performing a sinusoidal temperature change at 34.72 µHz. So, a strong signal component is expected at 34.72 µHz, whereas the minor components are expected to come from the system. In the case of η_2, higher-order tones are less than the 3% amplitude value of the dominant excitation tone. Unexpectedly, η_1 shows 10 dominant frequency components with tripled frequency component 126% higher than the excitation tone component. All amplitudes of η_1 from 1·34.72 µHz to 3·34.72 µHz are at least two times higher than in η_2.

Regarding Equations (3) are reassembling differential signals, it leads to the conclusion that quadrant signals of QPD1 get mixed with an additional signal in detection bandwidth.

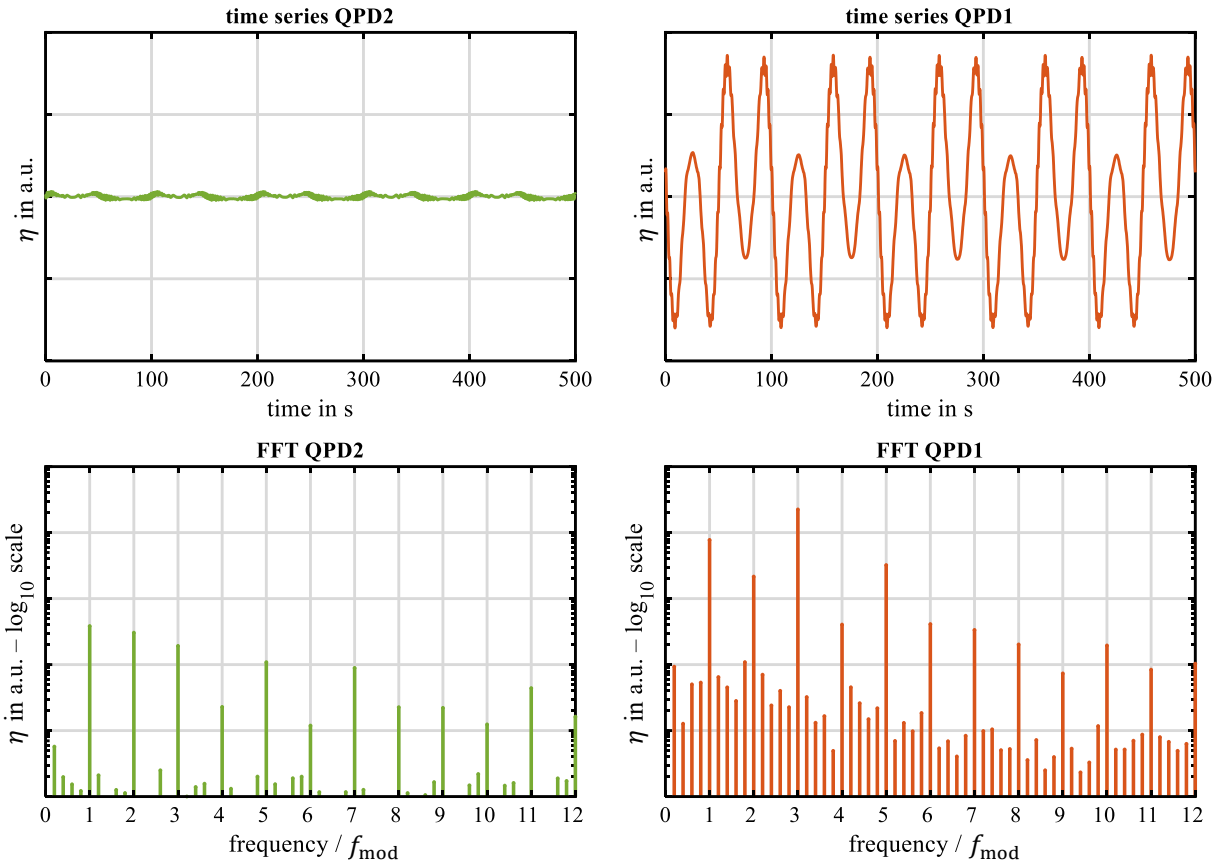

Figure 4: DWS signals detected by QPD2 (left) and QPD1 (right) while modulation the laser frequency (stabilized temperature). The upper plots show the time-domain signals while the lower plots show the FFT amplitude spectra (amplitudes rescaled by 288 (= 8 h/100 s)). During this data set, $f_{\mathrm{mod}} = 10$ mHz is used to modulate the laser frequency. Both time-domain plots show higher order frequency components. FFT plots show dominant harmonics up to 12. For QPD2, the highest amplitude is at excitation tone. In contrast to QPD1, where the highest amplitude is at 3rd harmonics. Overall, QPD2's noise floor is smaller than QPD1's together with smaller corresponding amplitudes at the same harmonic number. (Data from [3][4]).

Besides modulating the system with a thermal tone, the setup is capable of operating with modulated laser frequency f. As expected for an unequal arm-length interferometer, ΔL shows a proportional modulation. For differential signals monitoring the wavefronts of the system, these signals should be almost zero. The setup's characteristics can be estimated from this type of measurement.

Figure 4 depicts the DWS signals of both QPDs as time-domain signals and corresponding amplitude spectra derived from FFT. QPD2's signal shows a small time-domain amplitude compared to QPD1, as well as both QPD plots in Figure 3. The amplitude spectra show highly dominant harmonics compared to the noise floor contributions. This noise floor structure is different compared to Figure 3 noise amplitudes being smaller for Figure 4 at same harmonic number. Similar to Figure 3, higher harmonics of QPD2's spectra are always smaller than excitation tone. QPD1's time-domain signal was inverted to highlight the high similarity between upper right plots in Figure 3 and Figure 4. In FFT plot, the amplitudes of 1st and 2nd harmonic are both at least 289% less than 3rd harmonic amplitude (Figure 4). This ratio is higher than in the measurement of Figure 3 with 126%. The corresponding noise floor is smaller Figure 4 than in Figure 3.

3.2 Free-spectral range analysis

As mentioned in the previous subsection, the both signals in Figure 4 should be almost zero because the wavefronts of reference beam and measurement beam are not tilted physically during f modulation. QPD2's signal more closely replicates this ideal behavior as compared with QPD1's signal. Weak reflections in the system and misalignment of reference beam and measurement beam on each individual detector does not fully explain the frequency dependency of DWS signals and needs further investigations.

While modulating the frequency, characteristic frequencies of etalons between optical surfaces can be detected as an ansatz. Performing a frequency modulation, e. g. Figure 4, allows to calculate free-spectral range FSR. This formula can be modified to calculate etalon length L'

$$L' = \frac{c}{2\,FSR} \tag{4}$$

with c as speed of light in vacuum ($c = 299\,792\,458\ \mathrm{m/s}$ [10]).

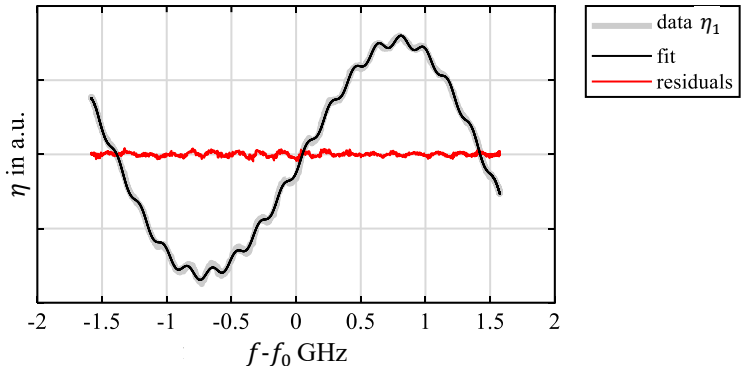

Figure 5: DWS signal of QPD1 plotted over laser frequency (x-y plot using time for synchronization) with $f_0 = 281.6286\,THz$, a fitted sine model and residuals. (Data from [3][4]).

QPD2's signal resembles expected system behavior in Figure 3 and Figure 4, the following analysis focus more on QPD1's signal. Figure 5 shows QPD1's DWS signal over modulated laser frequency. A non-linear least square fit with a sum of four sine waves of the data (see Appendix on page 8 for details) was performed and is also displayed in Figure 5. The corresponding fit's residuals show a similar size as η_2 in Figure 4 and will considered as system characteristic.

Combining fit and Equation (4) lead to $L'_1 = 51.7\ \mathrm{mm} \pm 0.8\ \mathrm{mm}$, $L'_2 = 103.6\ \mathrm{mm} \pm 2.7\ \mathrm{mm}$, $L'_3 = 820\ \mathrm{mm} \pm 0.5\ \mathrm{mm}$. One finds that L'_1 differs by an approximate factor of two to L'_2. However, L'_3 can be roughly estimated as distance in the real optical setup of the interferometer between M1 and a beam splitting cube.

Length L'_1 agrees well with the value found in our previous publication [3]. There we used length variation ΔL, frequency variation Δf and frequency mean value f to derive the sample's length as $52.33\ \mathrm{mm} \pm 0.02\ \mathrm{mm}$ with Equation (5):

$$L = f\frac{\Delta L}{\Delta f} \tag{5}$$

Both numbers are nearly the same and have an overlapping uncertainty interval. Both sample mirrors M1 and M2 being L apart, lead to the assumption that an incidence near these mirrors is causing the higher harmonics pattern of η_1. The beam path is highly symmetric in all other parts of the setup (see Figure 1 for reference).

As mentioned in publication [4] and shown in Figure 6, there are two hypotheses for this behavior: etalon (Subsection 3.3) or clipping (Subsection 3.4). Both hypotheses will be discussed in the following.

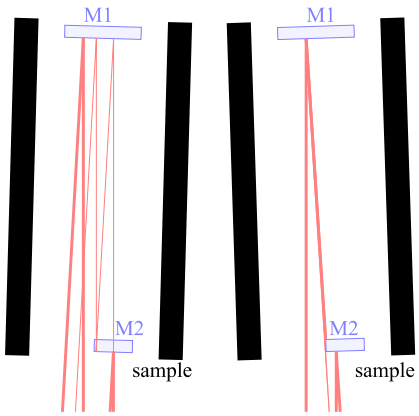

Figure 6: Schematic drawing for etalon and clipping hypothesis. In etalon hypothesis (left), a beam portion is transmitted through M2 and reflected together with main beam from M1. Depending on the sample's tilt, multiple "ghost" reflections are possible. In clipping hypothesis (right), the reflected beam from M1 is partially blocked by M2. (Original from [4]).

3.3 Etalon hypothesis

An etalon can form if the beam reflected at M2 is partially transmitted towards M1. The mirror in the sample has a polished back to simplify the adjustment process. The "leaking beam" is then reflected at the highly reflective coated surface of M1. As depicted in Figure 6 (left), the "leaking beam" undergoes multiple reflections off M1 and M2.
Using the results of Figure 5, a single bounce off and transmission as a "ghost beam" together with the "main beam" is expected. Both beams then interfere at QPD1 with the reference beam. The "ghost beam" possibly affects the differential character of DWS detection.

3.4 Clipping hypothesis

Beam clipping was suspected in our previous publications [3][4]. This hypothesis is supported by the fact that the space for passing M2 is the tightest in the setup. It is depicted in Figure 7. The dimensions span a half-circle of 11 mm in diameter and 5.5 mm in radius in contrast to a doubled beam diameter of approximately 5 mm.
The beam to M1 passes M2 without clipping. Particularly, the beam reflected off M2 is not clipped. After reflecting off M1 the beam gets diffracted at M2. Exemplary, Figure 6 (right) shows M2 is partially blocking the beam path. The resulting beam detected by QPD1 will have a distorted wavefront and presumable shapes η_1's waveform in both measurements.

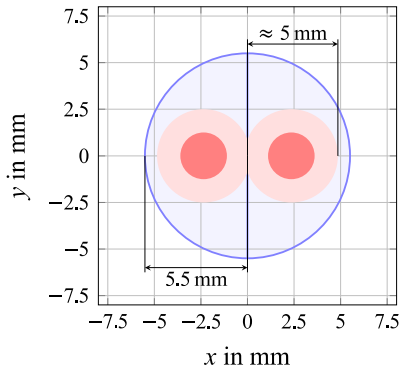

Figure 7: Schematic drawing of dimensions inside sample tube. Mirrors M1 an M2 in blue and laser beam with doubled diameter in light reds.

4. CONCLUSION

In this paper, we presented a review of former publications on our dilatometer setup. The focus of this paper was the frequency-based analysis of DWS signals of a silicon sample. We reused existing data to present two hypotheses: etalon and clipping occurring in our sample tube in more detail.
The analysis was carried out based on two sets of data: One at stabilized laser frequency and modulated temperature and another at modulated laser frequency and stabilized temperature. The second data set was used for further analysis in terms of free-spectral range. Using a resulting fit and comparing it with a method from our previous publications makes a distortion event between both sample mirrors trustworthy. Evolving the idea with a free-spectral range further, feeds the etalon hypothesis in both data sets. In contrast, the clipping hypothesis rely additionally on mechanical dimensions in our setup.
Further measurements in the lab and simulation have to show if one or both withstand repeating execution, (thermal) cycling, and setup adjustments.

APPENDIX: SINE-WAVE APPROXIMATION

In Subsection 3.2 a sine fit was used to derive FSR. Here, a more detailed description is given. The transmission equation for etalons can be found in various literature (e. g. [11])

$$T = \frac{1}{1 + F \sin^2(\delta/2)} \tag{6}$$

with coefficient of finesse $F = 4R/(1-R)^2$ using R as reflectance and δ as phase difference

$$\delta = 2\pi f \frac{2L}{c} \cos(\alpha) = 2\pi f \frac{2L'}{c} = 2\pi f \frac{1}{FSR} \tag{7}$$

In the first term of Equation (7), α represents the angle between the beam and the surface this beam is interacting with. Combining L and $\cos(\alpha)$ to L' which represents an effective length in the context of the etalon. Using Equation (4), the term can be further substituted to implement FSR.
Assuming M2's backside reflectance being low (only polished) and so $F < 1$, a linear approximation of Equation (6) leads to

$$T = 1 - F \sin^2(\delta/2) = 1 - F/2 \cdot (1 - \cos(\delta)) \tag{8}$$

together with Equation (7) a fit using $\text{offset} + \text{amplitude} \cdot \sin(2\pi f/FSR + \text{phase})$ can be applied.

REFERENCES

[1] J. Codero, T. Heinrich, T. Schuldt, M. Gohlke, S. Lucarelli, D. Weise, U. Johann, and C. Braxmaier, "Interferometry based high-precision dilatometry for dimensional characterization of highly stable materials," Measurement Science and Technology, IOP Publishing, pp. 1-10, 2009.

[2] R. Spannagel, I. Hamann, J. Sanjuan, T. Schuldt, M. Gohlke, U. Johann, D. Weise, and C. Braxmaier, "Dilatometer setup for low coefficient of thermal expansion materials measurements in the 140 K-250 K temperature range," Review of Scientific Instruments, AIP Publishing, pp. 1-8, 2016.

[3] I. Hamann, J. Sanjuan, R. Spannagel, M. Gohlke, G. Wanner, S. Schuster, F. Guzman, and C. Braxmaier, "Laser-dilatometer calibration using a single-crystal silicon sample," International Journal of Optomechatronics, Taylor & Francis Group, pp. 18-29, 2019.

[4] I. Hamann, "Charakterisierung dimensional hochstabiler Werkstoffe für die Raumfahrt mit hochauflösender Laser-Dilatometrie," Dissertation, Universität Bremen, pp. 1-135, 2020.

[5] G. Wanner, G. Heinzel, E. Kochkina, C. Mahrdt, B.S. Sheard, S. Schuster, and K. Danzmann, "Methods for simulating the readout of lengths and angles in laser interferometers with Gaussian beams," Optics Communications, Elsevier, 4831–4839, 2012.

[6] http://www.lisa.aei-hannover.de/ifocad/

[7] T. Schuldt, C. Braxmaier, H. Müller, G. Huber, A. Peters, and U. Johann, "Frequency stabilized Nd:YAG laser for space applications," Proceedings of the International Conference on Space Optics, SPIE, pp. 1-8, 2019.

[8] G. Wanner, S. Schuster, M. Tröbs, and G. Heinzel, "A brief comparison of optical pathlength difference and various definitions for the interferometric phase," IOP Publishing, pp. 1-5, 2015.

[9] H. Müller, S.-W. Chiow, Q. Long, C. Vo, and S. Chu, "Active sub-Rayleigh alignment of parallel or antiparallel laser beams," Optics Letters, Optica Publishing Group, pp. 3323-3325, 2005.

[10] Bureau international des poids et mesures "Proceedings of the 26th CGPM (2018)," https://www.bipm.org/documents/20126/17314988/CGPM26.pdf, pp. 1-472 (c from p. 203), 2019.

[11] D.G. Smith, "Field Guide to Physical Optics," The field guide series; FG17, Society of Photo-Optical Instrumentation Engineers (SPIE), pp. 28-29, 2013

CONTACTS

Dr.-Ing. I. Hamann — email: ines.hamann@dlr.de

Lee Kumanchik, Ph.D. — email: lee.kumanchik@dlr.de; ORCID: https://orcid.org/0000-0002-6688-2582

Dr. Gudrun Wanner — email: gudrun.wanner@aei.mpg.de; ORCID: https://orcid.org/0000-0001-5578-1471

Martin Gohlke — email: martin.gohlke@dlr.de

Josep Sanjuan, Ph.D. — ORCID: https://orcid.org/0000-0002-3570-5735

Prof. Dr. Claus Braxmaier — email: claus.braxmaier@dlr.de, claus.braxmaier@uni-ulm.de; ORCID: https://orcid.org/0000-0002-5640-1634